Supplementary Information

Tuning Hardness in Calcite by Incorporation of Amino Acids

Yi-Yeoun Kim[1]*, Joseph D. Carloni[2], Beatrice Demarchi[3], David Sparks[4], David G. Reid[5], Miki E. Kunitake[2], Chiu C. Tang[6], Melinda J. Duer[5], Colin L. Freeman[4], Boaz Pokroy[7], Kirsty Penkman[3], John H. Harding[4], Lara A. Estroff[2,8], Shefford P. Baker[2]* and Fiona C. Meldrum[1]*

Content:

Supplementary Methods

Materials. $CaCl_2 \cdot 2H_2O$, $(NH_4)_2CO_3$, sodium L-aspartate and glycine were purchased from Sigma-Aldrich, while glycine (1-13C and 2-13C) and L-aspartic acid (3-13C and 1,4-13C 99%) were purchased from Cambridge Isotope Laboratories Inc. All chemicals were used without further purification.

$CaCO_3$ precipitation. The two amino acids, Asp and Gly, were mixed with 2 – 100 mM aqueous solutions of $CaCl_2.2H_2O$ to give amino acid concentrations of 0.001 – 100 mM Asp and 0.1 - 400 mM Gly. 40 mL of the prepared solutions were transferred to plastic Petri dishes (90 mm) containing glass slides, which had previously been cleaned with Piranha solution (H_2SO_4 70 vol% H_2O_2 30 vol%), and $CaCO_3$ was precipitated using the ammonium carbonate diffusion method.[1] This was achieved by covering the Petri dishes with Parafilm pierced with multiple holes and placing them in a dessicator previously charged with 5 g of freshly crushed $(NH_4)_2CO_3$ powder. Crystallisation was then allowed to proceed for 2 days (unless otherwise stated), after which time the glass slides were removed from solution, washed thoroughly with Millipore water and ethanol, and oven-dried (40 ^oC) prior to further characterization.

$CaCO_3$ precipitation in the presence of 400 mM Gly took longer than 2 days; this was the maximum concentration of Gly employed. In the case of Asp, a mixture of single crystal and polycrystalline particles formed at Asp concentrations above 50 mM, and principally polycrystalline particles formed above 100 mM Asp (Supplementary Fig. 1). The maximum Asp concentration employed was therefore 50 mM. Investigation of the influence of the initial Ca concentration in solution showed that while higher initial Ca concentrations favour occlusion of the amino acids (Figs. 2c and 2d), they also drive the generation of

polycrystalline calcite at lower Asp concentrations (Supplementary Fig. 2). For example, at an initial [Ca] = 25 mM, polycrystalline calcite was observed at 25 mM Asp (Supplementary Fig. 3). An initial [Ca] = 10 mM was therefore chosen as the standard condition as this offered efficient occlusion of the amino acids, while still retaining single crystallinity of calcite upto wide range of amino acid concentration..

Calcite crystals were also precipitated in the presence of 13C-labelled Asp and Gly such that they could be analyzed in Proton driven spin diffusion (PDSD) experiments to determine the proximities of the occluded amino acids. Calcite/Asp crystals were precipitated from solutions of concentrations [Ca^{2+}] = 10 mM and [1,4-$^{13}C_2$ Asp] = [3-^{13}C Asp] = 25 mM, while calcite/Gly crystals were precipitated from solutions of [Ca^{2+}] = 10 mM and [1-^{13}C Gly] = [2-^{13}C Gly] = 100 mM.

Quantification of the incorporation of amino acids within calcite crystals. All calcite samples were bleached in 12% w/v sodium hypochlorite for 48 hrs before analysis using 50 μL of hypochlorite per mg of calcite. This effectively removes surface-bound amino acids, as demonstrated during the characterisation of biomolecules occluded within a range of biominerals[2-4] The amino acids were then extracted from the $CaCO_3$ crystals by dissolving them in cold 2 M HCl (using a minimum of 10 μL HCl per mg of calcite). The acid was then evaporated and the samples rehydrated with an adequate volume of a rehydration fluid containing 0.01 mM HCl, 0.77 mM sodium azide at pH 2, and an internal standard (0.01 mM L-homo-arginine). The rehydrated samples were analyzed for chiral amino acids on an automated reverse-phase high-performance liquid chromatography (RP-HPLC) system equipped with a fluorescence detector, using a modification of the method of Kaufman and Manley[5]. In brief, 2 μL of rehydrated sample was mixed online with 2.2 μL of derivatizing reagent (260 mM N-isobutyryl-l-cysteine, 170 mM o-phthaldialdehyde, in 1 M potassium

borate buffer, adjusted to pH 10.4 with KOH) immediately before injection. This set-up is optimized for the routine separation of enantiomeric pairs, which is achieved on a C18 HyperSil BDS column using a gradient elution of sodium acetate buffer (pH 6.00 ± 0.01), methanol, and acetonitrile. Quantification of the amounts of Asp and Gly occluded within the calcite crystals was achieved using calibration curves, as reported in[6] using the (normalized) RP-HPLC peak areas, taking into account the mass of the calcite sample analyzed and the volume of rehydration fluid used.

Characterization of amino acid/calcite composite particles. The crystals were analyzed using Scanning Electron Microscopy (SEM), optical microscopy, and selected samples were also analyzed using synchrotron X-ray powder diffraction. For SEM, particles on glass substrate were mounted on aluminum stubs using carbon sticky pads, and were coated with 5 nm Pt/Pd using FEI Nova NanoSEM.

Solid state nuclear magnetic resonance (ssNMR) spectroscopy analysis. All ssNMR spectra were recorded on a Bruker Avance I NMR spectrometer with a 9.4 T superconducting magnet, operating at 400 MHz for ^{1}H and 100 MHz for ^{13}C. Samples were packed into 4 mm zirconia rotors, with Teflon tape being used to fill out empty space within the rotor. Magic angle spinning (MAS) rate was 10 kHz. The standard cross polarization (CP) sequence in the Bruker pulse program library was used; ^{1}H 90° pulse length 2.5 μs, contact time 2.5 ms, with a ramped pulse on ^{1}H and spin lock field 70 kHz. During acquisition, spinal64 decoupling at 100 kHz RF field strength was applied on ^{1}H. Repetition time was 2 s between successive acquisitions to allow relaxation.

Proton driven spin diffusion (PDSD) experiments were conducted using the same initial cross polarization parameters as employed in the ^{13}C CP experiments. At 10 kHz

MAS, the magnetization was allowed to evolve at single-quantum coherence during the incremental delay (t_1), and returned to zero quantum coherence by a ^{13}C 90° pulse of 3.8 μs. ^{1}H decoupling was switched off during this mixing period of 100 ms to allow transfer of ^{13}C magnetization via dipolar coupling and spin diffusion[7] with a ^{13}C 90° readout pulse at the end of the mixing period. During both the incremental delay and acquisition periods, spinal64 decoupling was applied at 100 kHz. The pulse sequence used was an adapted version of the Avance I CP spin diffusion experiment in the Bruker library.

Synchrotron powder X-ray diffraction (PXRD) analysis. The high-resolution PXRD measurements were carried out on the synchrotron beamline (I11) at Diamond Light Source Ltd, Didcot, UK. Instrument calibration and wavelength refinement (λ=0.8257156(10) Å) were performed using high quality NIST silicon powder (SRM640c) and instrumental contribution to the peak widths does not exceed 0.004^{o8}. Diffractograms were recorded from the specimens at room temperature. Sample powders for analysis were loaded into 0.7 mm borosilicate glass capillaries, and to avoid intensity spikes from individual crystallites, the samples were rotated during measurements at a rate of 60 rps. PXRD data was then obtained using high-resolution MAC (multi-analyzer crystal) diffraction scans, with scan times of 1800 s.

The structural parameters were refined by Rietveld analysis using GSAS and PANalytical X'Pert HighScore Plus software. Lattice distortion, strain and size analysis was performed using both Rietveld analysis for whole spectrum and line profile analysis for the (012), (104), (001), (110) and (113) reflections using PANalytical X'Pert HighScore Plus software. Goodness of fitness values for all the analyzed samples are summarized in Supplementary Tables 1 and 2.

To analyze peak shape, peak broadening was expressed as FWHM and Integral Breadth. (Fig. 3 and Supplementary Figs 4 and 5) Total FWHM is the full width at half maximum for each of the peaks, while Integral Breadth is the width of a rectangle that can be placed within the peak that has the same area as the net peak area, (Net area/net height). Microstrain (%) is derived by line profile analysis and shows the microstrain contribution to the total line broadening. Coherence length (nm) is derived by line profile analysis and shows the coherence length contribution to the total line broadening (Supplementary Fig. 4).

Mechanical testing. Cyanoacrylate resin was poured over glass slides supporting precipitated calcite/amino acid crystals and was then allowed to set overnight. The resin and crystals were polished using graded Al_2O_3 lapping films and a final 50 nm Al_2O_3 powder (Buehler micropolish γ–Al_2O_3) suspended in a water and 2-methyl-2,4-pentanediol mix (Green Lube, Allied High Tech) until the crystals were exposed for measurement (Supplementary Fig. 8). The surface roughness of samples produced following this protocol was less than 10 nm RMS as determined using the indenter tip as a scanning force probe.

Nanoindentation measurements were performed on exposed calcite/amino acid crystals with in-plane sizes of 20–60 μm using a Berkovich (≈120 nm tip radius) diamond indenter in a commercial nanoindenter system (Hysitron TriboIndenter 900). Before data collection, the shape of the tip was calibrated using the method of Oliver and Pharr[9]. Each indent consisted of five-second load, hold, and unload segments with a maximum load of 2500 μN, resulting in ≈200 nm deep indents. The unloading segment was used to calculate the indentation modulus and hardness[9]. The maximum load was chosen to create an indentation large enough to sample a homogeneous volume and minimize the effects of surface roughness, while allowing multiple indents per sample. Surface topography scans

were performed with the indenter tip before and after indenting to ensure indentations were located at least 5 μm away from any edges.

The hardness and modulus of calcite depends on the orientation of the crystal with respect to the nanoindenter tip. For example, for indentations on the {001} facet of calcite, the hardness ranges from 2.3 to 2.5 GPa and the indentation modulus ranges from 68 to 77 GPa with azimuthal angle[10]. For randomly oriented crystals, averaging over multiple crystals with multiple indentations provides an average hardness and modulus over a range of crystallographic orientations. In this work, 5 to 8 different randomly-oriented crystals were selected for each growth condition, and 4-10 indentations were made per crystal, resulting in at least 28 measurements for each amino acid concentration.

Supplementary Note 1. Simulation protocols

The program Packmol[11] was used to place the amino acids inside the crystal in a random orientation for a range of 0-2.3 mol% (Asp^{1-}, Gly^{0}) or 0-3.2 mol% (Asp^{2-}, Gly^{1-}) of amino acid within the simulation box, corresponding to a maximum inclusion of 3.5, 3.9, 4.8 or 5.5 wt% for Asp^{1-}, Gly^{0}, Asp^{2-} and Gly^{1-} respectively. To avoid a net charge change in the system the solution chemistry shown in supplementary equations 1-4 was used. In all systems the calculations of the energetics of the excess Ca^{2+} and CO_3^{2-} ions were made with respect to bulk calcite such that our results did not depend on the reference state of the system.

$$Ca^{2+}(aq) + Asp^{2-}(aq) + Ca^{2+}(crystal) + [CO_3]^{2-}(crystal) => 2Ca^{2+}(aq) + 2[CO_3]^{2-}(aq) + Asp^{2-}(crystal) + V_{Ca}^{2-}(crystal) + 2V_{CO3}^{2+}(crystal) \quad \textit{(Supplementary Eq. 1)}$$

$$Ca^{2+}(aq) + 2Gly^{-}(aq) + Ca^{2+}(crystal) + [CO_3^{2-}](crystal) => 2Ca^{2+}(aq) + 2[CO_3]^{2-}(aq) + 2Gly^{-}(crystal) + V_{Ca}^{2-}(crystal) + 2V_{CO3}^{2+}(crystal) \quad \textit{(Supplementary Eq. 2)}$$

$$Ca^{2+}(aq) + 2Asp^{-}(aq) + Ca^{2+}(crystal) + [CO_3^{2-}](crystal) => 3Ca^{2+}(aq) + 3[CO_3]^{2-}(aq) + 2Asp^{-}(crystal) + 2V_{Ca}^{2-}(crystal) + 3V_{CO3}^{2+}(crystal) \quad \textit{(Supplementary Eq. 3)}$$

$$Gly(aq) + Ca^{2+}(crystal) + [CO_3^{2-}](crystal) => 2Ca^{2+}(aq) + 2[CO_3]^{2-}(aq) + Gly(crystal) + 2V_{Ca}^{2-}(crystal) + 2V_{CO3}^{2+}(crystal) \quad \textit{(Supplementary Eq. 4)}$$

where V_X^y means a vacancy of $_X$ with the effective charge given in the superscript y.

The atomic charges for the amino acids were calculated with AMBER Antechamber[12] using the AM1-BCC method[13]. This uses a semi-empirical method in combination with bond charge corrections to calculate the electronic structure of the amino acid. For all simulations, the Molecular Dynamics package DL POLY Classic[14] was used and the mineral phase was described using the $CaCO_3$ potentials developed by Raiteri *et al.*[15] The interactions of the

organic molecules were described using the AMBER forcefield[16]. The interactions between the mineral and organic phase were modelled by using a generic method to produce cross term potentials[17], where this generated a reliable potential for our system without the need for further fitting.

All simulations were run at a temperature of 300 K and at atmospheric pressure (10^5 Pa). The simulations were equilibrated for 100 ps using a timestep of 0.1 fs for an NVT ensemble with a Nosé-Hoover thermostat[18]. Subsequent simulations were carried out for data analysis. These simulations were run in an NPT ensemble with a timestep of 1.0 fs using a Nosé-Hoover thermostat and a Hoover barostat[19] for 2.0 ns. The insertion energy of the amino acids was calculated using the solution chemistry as described in Supplementary equation (1-4) above. In order to calculate the configuration energy of the system under anisotropic expansion, simulations with a configuration of 5 mM Asp^- were performed to mimic the experimental setup. The simulation box was expanded manually and independently along either the *c*-axis or the *a*-axis (the *b* axis is equivalent to a-axis) in increments of 0.05 % of the initial lattice parameter per step. After each expansion, the configurational energy was calculated during a 0.5 ps simulation with a 1.0 fs timestep in an NVT ensemble.

Supplementary Note 2. Derivation of equation (1) to describe the hardness of calcite crystals with occluded amino acids

Of the slip systems in calcite, $\{\bar{1}02\}\ \langle 2\bar{2}1\rangle^{+/-}$, $\{104\}\ \langle\bar{2}21\rangle^{+/-}$ and $\{\bar{1}08\}\ \langle 401\rangle^{+/-}$ have the lowest critical resolved shear stresses [20]. The $\{\bar{1}02\}$ and $\{104\}$ systems have large Burgers vectors and require high temperatures and/or pressures to operate, while the $\{\bar{1}08\}$ twinning system can be activated in uniaxial loading at room temperature and pressure[20]. Since at least 5 independent slip systems are needed for generalized

plasticity, as required to form the indentations (Fig. 6a), it is evident that the pressure under the indenter is sufficient to activate the more difficult of these slip systems.

To determine the form of the relationship between H and F_c, we first estimate the dislocation line tension T from $T = \alpha G b^2$ where G is the shear modulus and b is the magnitude of the Burgers vector. Taking $\alpha = 1$, $G = 35$ GPa, and $b = 0.5$ nm (G and b calculated as averages for the material), we find $T \approx 9$ nN, which is significantly greater than the force required to break a covalent bond (estimated as 1.5 to 4 nN [21-23]), which in turn indicates that the angle θ at which the dislocation will cut the molecule will be low ($\leq 13^\circ$). Under these conditions, the critical resolved shear stress (τ_c) required for the dislocations cut the particles can be estimated from $\tau_c = (F_c/bL)\sqrt{F_c/2T}$, where L is the average separation of the molecules in the lattice[24]. To convert τ_c to H, we use known critical resolved shear stresses for the slip systems in calcite[20] and our measured indentation modulus to estimate a yield stress (Y) to modulus (E) ratio of ≈ 0.01. Finite element simulations indicate that H approaches $2.8Y$ for materials with $Y/E < 0.02$[25]. Using this relationship, and the von Mises criterion to relate Y to τ_c, the hardness is related to the critical resolved shear stress by $H \approx 4.8\tau_c$. If we assume that strength of the crystal is just the sum of the intrinsic resistance to dislocation motion (as determined from the hardness, H_0, of pure Iceland spar) and the additional strengthening due to AA molecules, we can write the result as Equation 1.

$$H = H_0 + 4.8(F_c/bL)\sqrt{F_c/2T} \qquad \text{(Equation 1)}$$

Supplementary Note 3. Estimation of lattice misfit of AA molecules in calcite

One distinction between solutes and second phase particles is their effect on lattice strains. A solute species has a certain size and replaces a fundamental unit of the host crystal that also has a certain size (or is inserted interstitially). Unless the solute and the space in the lattice into which it is inserted happen to be the same size and shape, accommodation strains are required *e.g.* when Mg^{2+} is substituted for Ca^{2+} in calcite[26-30]. In contrast, both a second phase particle and the space created for it in the crystal may consist of many formula units (atoms or molecules) which can be closely adjusted so that little or no lattice strains are required, *e.g.* ~ 200 nm polystyrene inclusions in calcite[31].

With respect to lattice distortions, amino acid inclusions behave like solutes. The closest fit for Gly^0 is achieved when it replaces one $CaCO_3$ formula unit, and the closest fit for Asp^{2-} when it replaces one $CaCO_3$ unit and one CO_3^{2-} ion. Using molecular volumes for Gly^0, $CaCO_3$, Asp^{2-}, and CO_3^{2-}, of 0.077 nm^3 [32], 0.061 nm^3 [33], 0.13 nm^3 [34], and 0.055 nm^3 (found by subtracting the volume of a Ca^{2+} ion, i.e. 0.0056 nm^3 [35], from that of $CaCO_3$), respectively, the misfit, expressed as $(r\text{-}r_0)/r_0$, where r and r_0 are the radii of spheres having the same volumes as the AA molecule and the space created for it in the lattice respectively, is 8.1% for Gly^0 and 3.9 % for Asp^{2-}. Similar calculations for $2Asp^{1-}$ and $2Gly^{1-}$ (as described in the simulations section) give misfits of 13.7 % and 9.9 %, respectively. It is noteworthy that not only do the strains from PXRD (Fig. 3) and simulations (Fig. 4) agree when Gly^0 and Asp^{2-} are considered as the occluding species, but the ratio of these strains is consistent with the ratio of the misfits, while any of the ratios including Gly^{1-} and Asp^{1-} are not. This suggests that the AA molecules are occluded as Gly^0 and Asp^{2-}, and not the paired molecules of Gly^{1-} and Asp^{1-} that were also considered in the simulations, in agreement with the NMR results.

These misfits result in large tensile strains in the calcite lattice in the neighborhood of each AA molecule, which drop off rapidly with distance from the molecule[36] (Fig. 3e). These distortions increase both the average lattice parameter (lattice distortions, Figs. 3a and 3b) and the inhomogeneity of the strains (microstrains, Figs. 3c and 3d and Supplementary Fig. 4). As $[AA]_{inc}$ increases, the strain fields around the molecules begin to overlap (note the small separation between molecules in Supplementary Fig. 9), and the strain inhomogeneity decreases as the lattice distortions continue to increase (Figs. 3e and 3f). Because the molecules are small and roughly equiaxed, the anisotropy in the lattice distortions (Figs. 3a and 3b) arises primarily from the elastic anisotropy of calcite (the stiffness along the *c* axis is 58% of that along the *a*-axis[37]).

Supplementary Note 4. Calculation of spacing, *L*, between amino acid molecules

As described in the main text, to determine the hardening mechanism of the amino acids, the spacing, *L*, between amino acid molecules within the calcite crystals must be determined. To calculate this value, we assume that the AA molecules are randomly distributed throughout the volume, consistent with the ssNMR data, and thus in any subset of that volume, such as a thin slice containing the slip plane. We convert the measured mole concentrations, $[AA]_{inc}$, to volume concentrations $C_{v,AA}$ (number of AA molecules/volume) using the known molecular volumes of calcite[33] and the amino acids in crystalline form[32,34] (there is very little difference between the polymorphs for our purposes). The number of AA molecules per unit area on the thin slice is then given by $C_{v,AA}*t$, where t is the thickness of the slice. Approximating the configuration of the molecules in the calcite as a square array, we have $L = (C_{v,AA}*t)^{-0.5}$. For geometric consistency, we set t equal to the diameter D_{AA} of

the AA molecule under consideration ($D_{AA} = \sqrt[3]{\frac{6v_{AA}}{\pi}}$, where v_{AA} is the volume of the amino acid), so

$$L = \left[C_{v,AA}\right]^{\frac{-1}{2}} \left[\frac{6v_{AA}}{\pi}\right]^{\frac{-1}{6}} \qquad \text{(Supplementary Equation 5)}$$

A plot of *L vs.* $[AA]_{inc}$ is shown in Supplementary Fig. 9.

Supplementary Note 5. The possible role of twinning.

Twinning is a common deformation mechanism in bulk calcite. However, it requires specific loading and boundary conditions, which are not provided in our tests. Furthermore, if twinning does occur, the resulting hardening is still expected to follow a rule like Eq (1). These ideas can be understood as follows. Although the $\{\bar{1}08\}$ twin system in calcite has a lower critical resolved shear stress than the $\{\bar{1}02\}$ and {104} slip systems, formation of a $\{\bar{1}08\}$ twin requires enormous shear strains (69.4%)[38] and thus occurs only where accommodations can be made for incompatibilities between the twin and the surrounding material. Accordingly, reports of twin deformation occurring underneath indentations in calcite fall into two categories:

(1) Cases where the incompatibility is accommodated by cracking or the presence of a free surface or other interface. For example, Li and Ortiz found a great deal of twinning under indentations in *P. placenta*, due to the presence of many compliant interfaces that could accommodate the large twin shear displacements[39]. In their indentation tests of pure calcite, few twins formed and these spanned relatively short distances between free surfaces, including the sample surface and subsurface cracks.

(2) Cases where the shear required to accommodate the indenter is matched to the shear required by the twin. For example, 2-D wedge indentations have been used to study "elastic twinning"[38]. For indentations made with a Berkovich indenter, slip on the $\{\bar{1}08\}$ system has been seen, but only on the {001} face at azimuthal angles where the interaction between the geometry of the indenter and the orientation of the crystal, along with the free surface and the formation of cracks, allowed it[10].

We know of no study in which twins have been reported underneath indentations in single crystal calcite where no cracking (or other accommodating interface) was present.

Furthermore, our experiments revealed no evidence of twinning in either the load-displacement data (*e.g.* "pop-in" events[39]) or in the surface profiles (Fig. 6a inset).

This discussion does not prove that twinning did not occur in our experiments. Even if there is twinning, however, twins grow by motion of "twin dislocations." These line defects can be more complicated than simple glide dislocations[40] but include a glide component that must interact with the occluded AA molecules. While new laws may be needed to account for temperature and rate dependence[41] the Friedel term in Eq 1 is geometric, and should apply equally well to full and twin dislocations in a comparative model such as ours (Eq. 1 compares the hardness of samples with and without occluded AA molecules subjected to identical tests). Thus, even if twinning occurs, we expect variations in hardness with AA content to follow Eq. 1 reasonably well.

Supplementary Figures

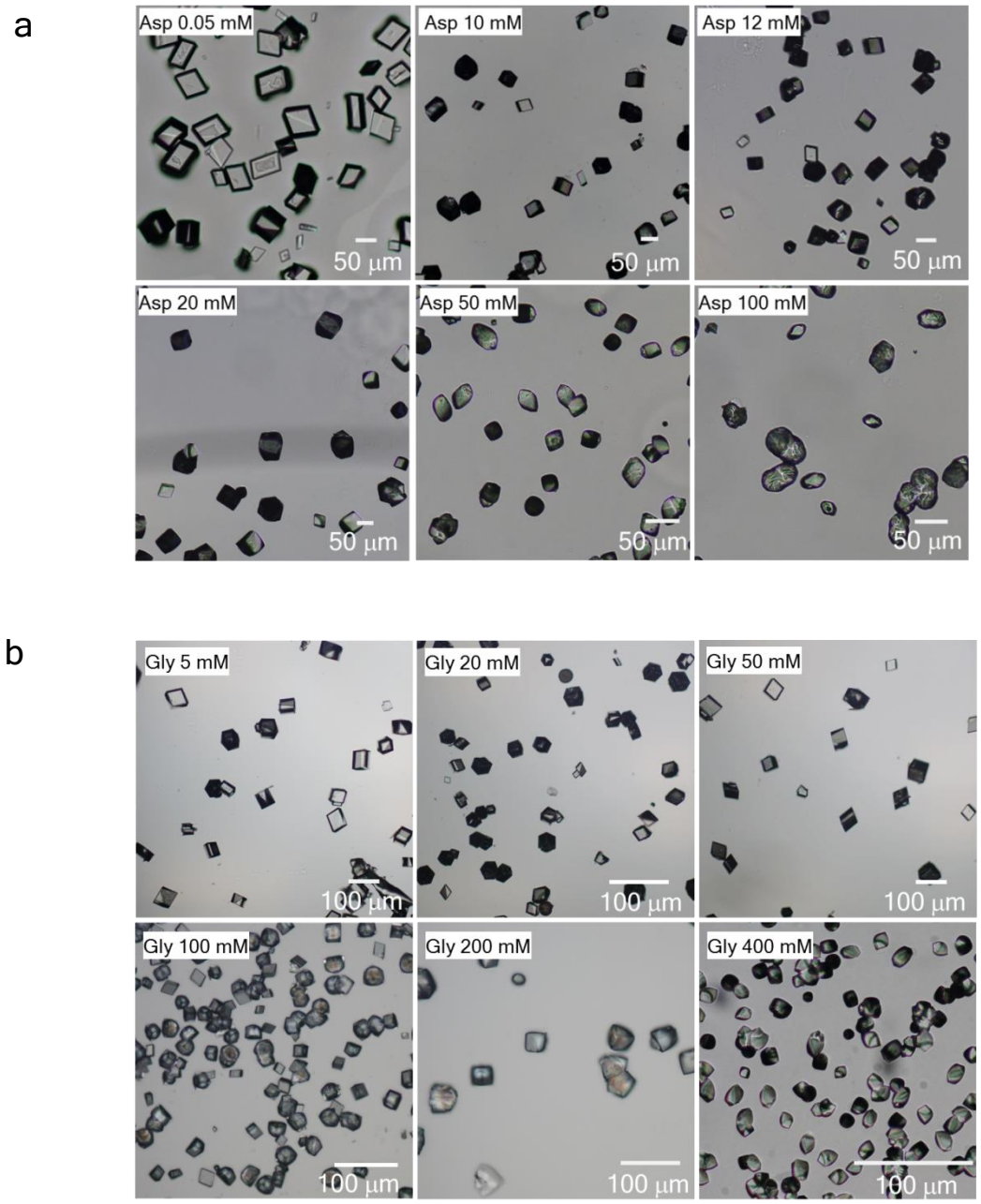

Supplementary Figure 1.

Optical microscope images of calcite crystals (a) showing morphological changes as a function of $[Asp]_{Sol}$ = 0.05 mM, 10 mM, 12mM, 20 mM, 50 mM and 100 mM. (b) shows morphological change as a function of $[Gly]_{Sol}$ = 5 mM, 20 mM, 50 mM, 100 mM, 200 mM and 400 mM. All the crystals were grown at an initial $[Ca^{2+}]$ = 10 mM. Note that the scale bars are individual to each figure and reflect the decrease in crystal size as the concentration of amino acid increases.

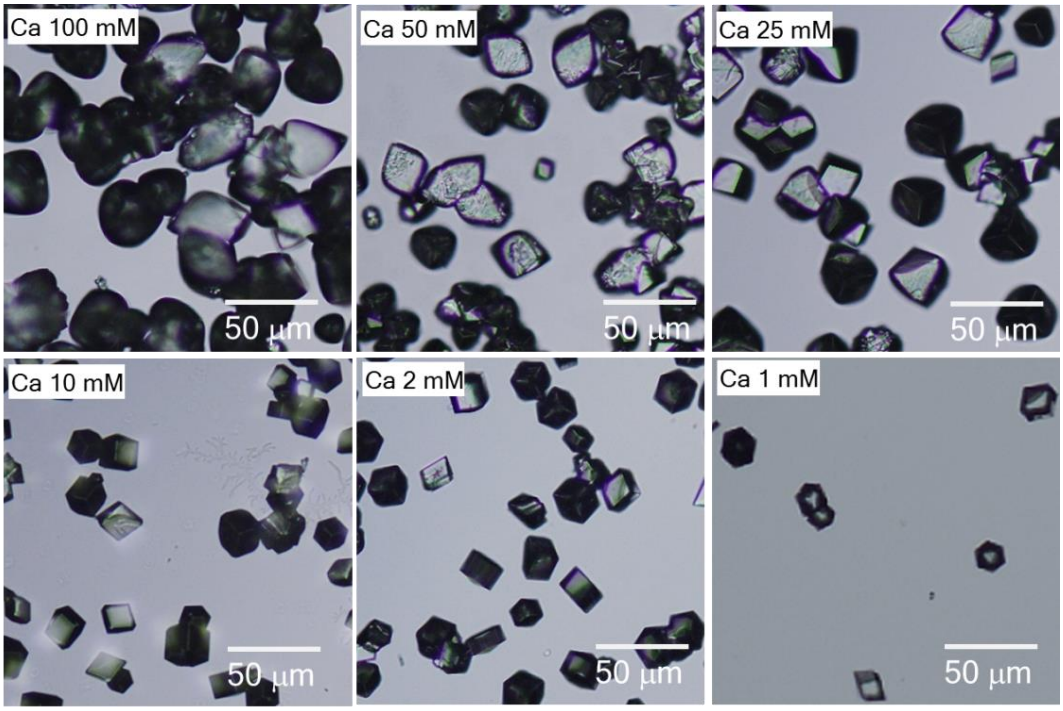

Supplementary Figure 2.

Optical microscope images of calcite crystals showing morphological changes as a function of the initial [Ca^{2+}] = 100 mM, 50 mM, 25 mM, 10 mM, 2 mM and 1 mM. All of the crystals were grown in the presence of an initial $[Asp]_{sol}$ = 10 mM.

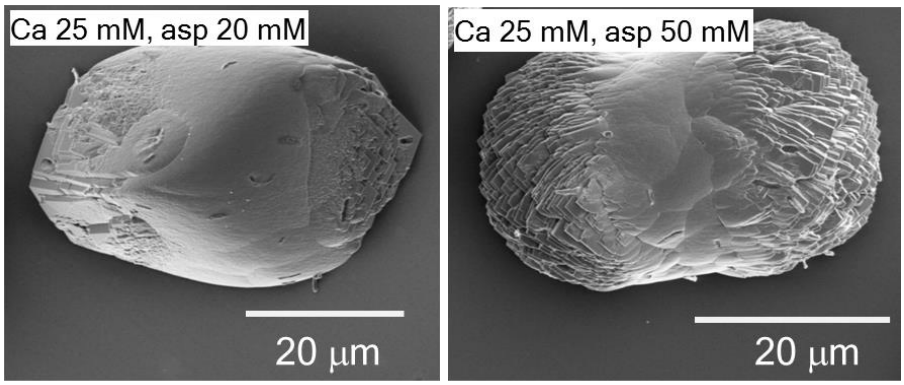

Supplementary Figure 3.

SEM images of calcite crystals grown at an initial [Ca^{2+}] = 25 mM showing a modified single crystal morphology at $[Asp]_{sol}$ = 20 mM, and a polycrystalline particle at $[Asp]_{sol}$ = 50 mM.

a

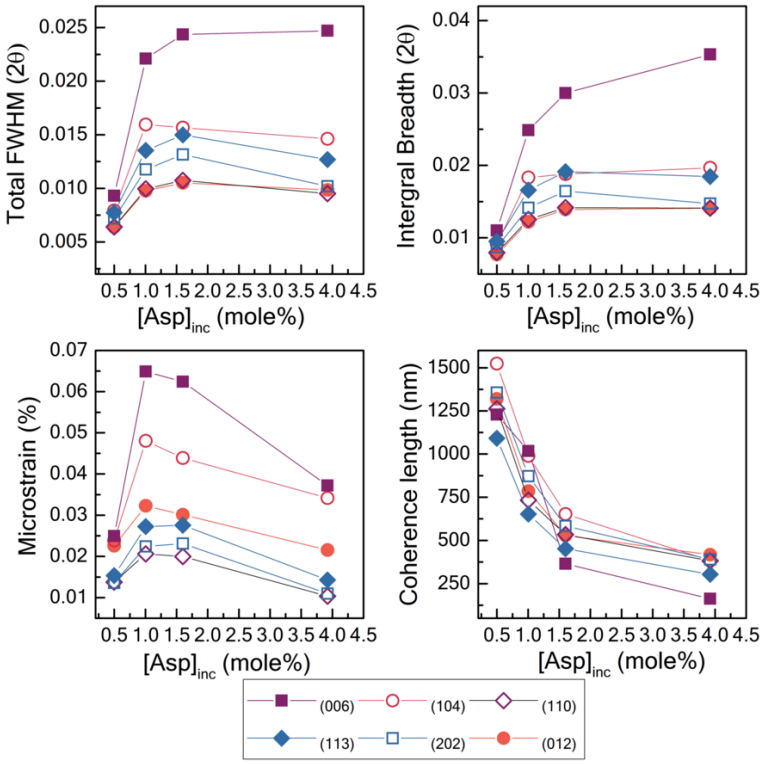

b

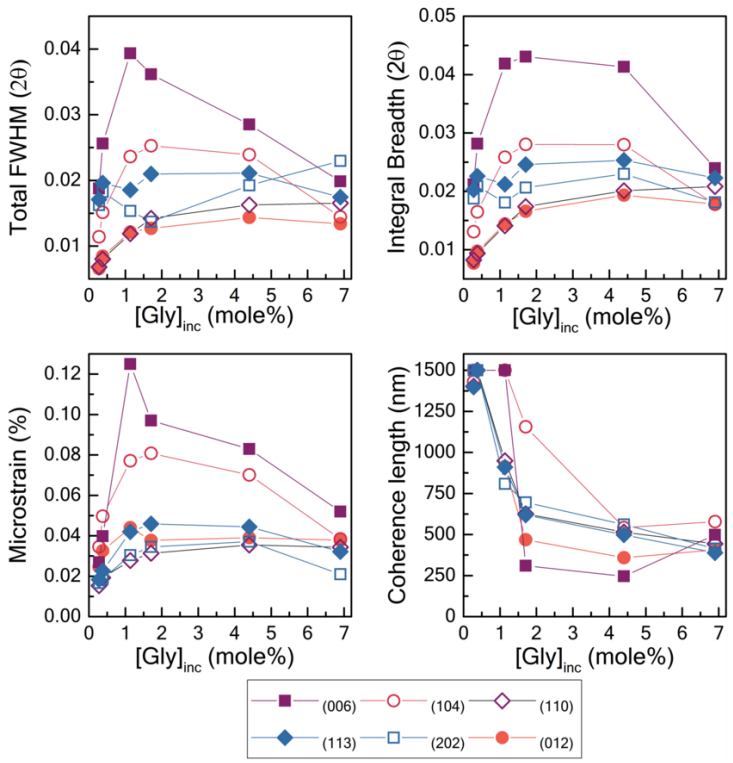

Supplementary Figure 4.

Changes in XRD peak Full Width at Half Maximum (FWHM), integral breadth, microstrain and coherence length induced by (a) Asp and (b) Gly incorporation.

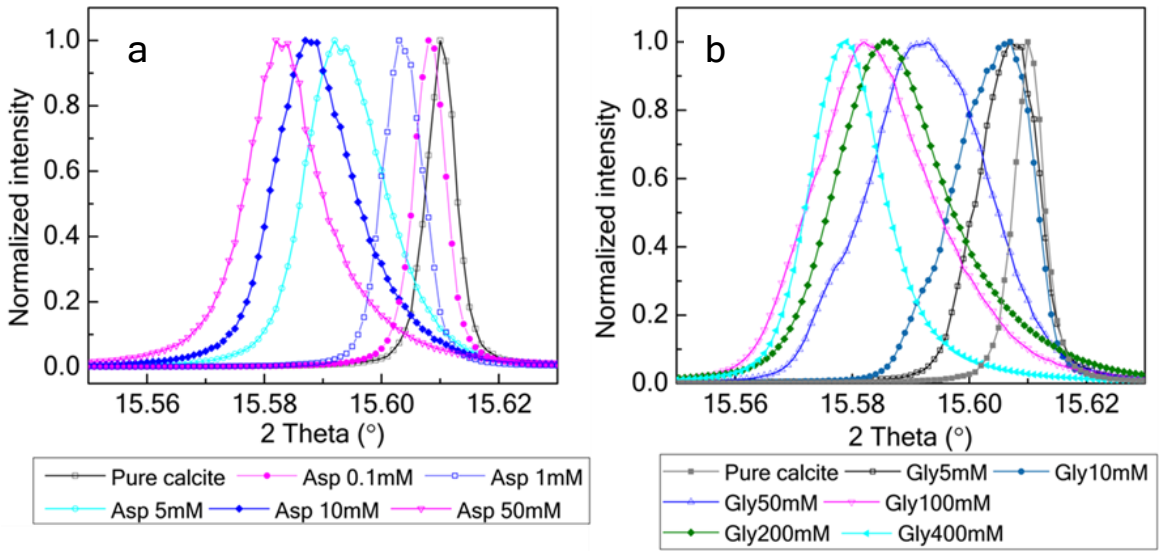

Supplementary Figure 5.

Changes in the positions and shapes of (104) reflections of the samples shown in Fig 3. The lattice shift and FWHM values of the peaks were shown in Fig 3. (A) The peaks shift to lower angles (higher d-spacings) with increasing occlusion of Asp, while at the same time increasing in width until [Asp] = 10 mM (1.67 mol %). The peak then becomes slightly more narrow at [Asp] = 50 mM. (B) The peaks shift to higher d-spacings with increased occlusion of Gly, while increasing in width until [Gly] = 50 mM, before narrowing again at higher values of [Gly].

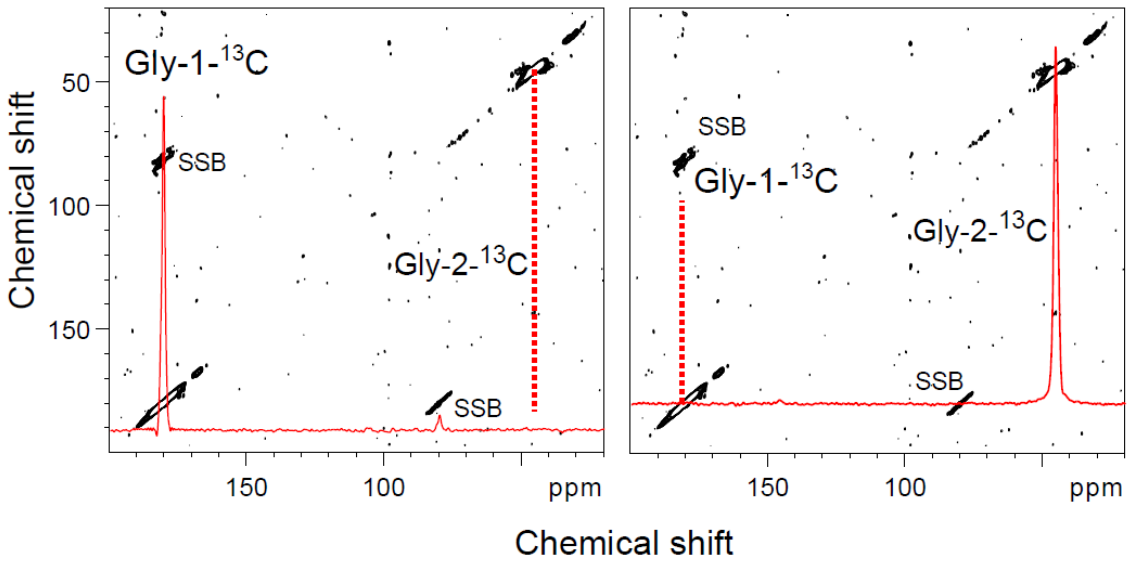

Supplementary Figure 6.

ssNMR showed no evidence for Gly-Gly intermolecular interactions or clustering. The black traces in each panel are (identical) contour plots of 2D proton driven spin diffusion (PDSD) data. The red traces depict rows extracted from the 2D plots at chemical shifts corresponding to the Gly-1C (left) and Gly-2C (right). If there were a detectable interaction between Gly neighbours we would see signals at the frequencies marked by dotted red lines in each trace, i.e. at the Gly-2C in the left panel, and Gly-1C in the right panel

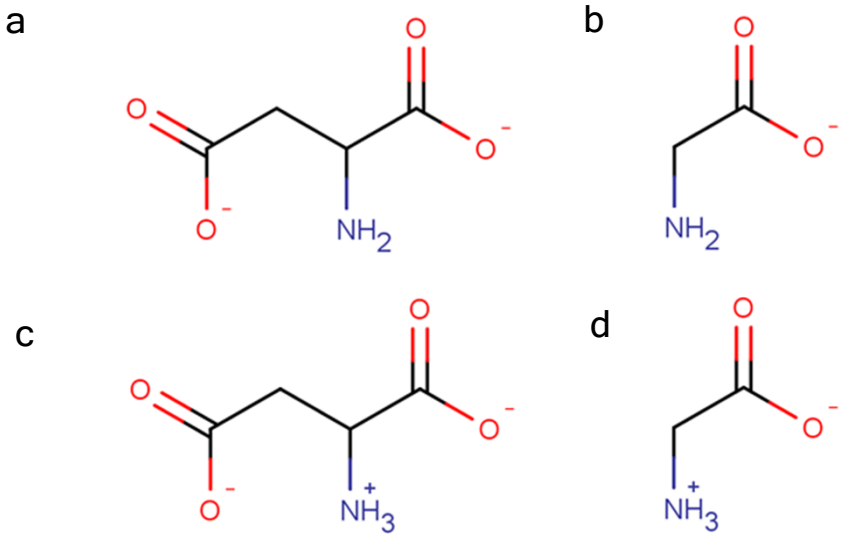

Supplementary Figure 7.

Chemical structures of the differently charged states of the aspartic acid and glycine used in simulations (a) Asp^{2-} (b) Gly^{1-} (c) Asp^{1-} (d) Gly^{0}.

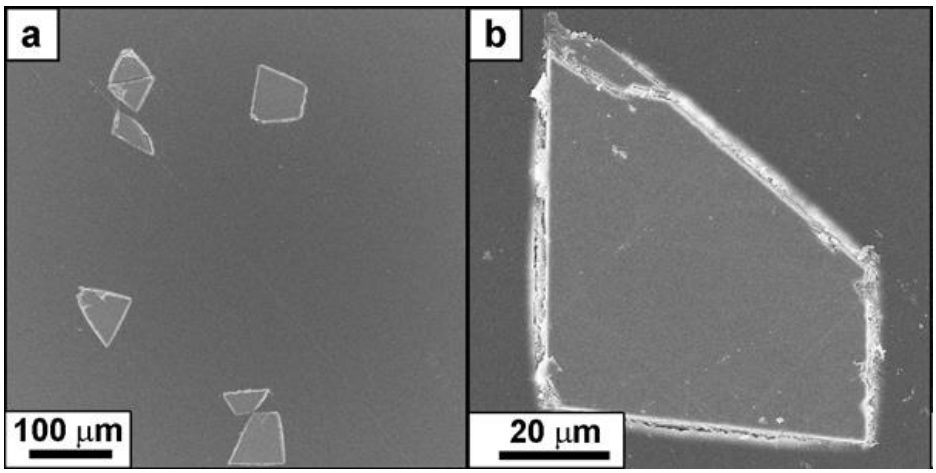

Supplementary Figure 8.

(a, b) Scanning electron micrographs of calcite crystals grown in the presence of [Asp] = 1 mM, embedded within cyanoacrylate resin, and polished to expose crystal surfaces for nanoindentation.

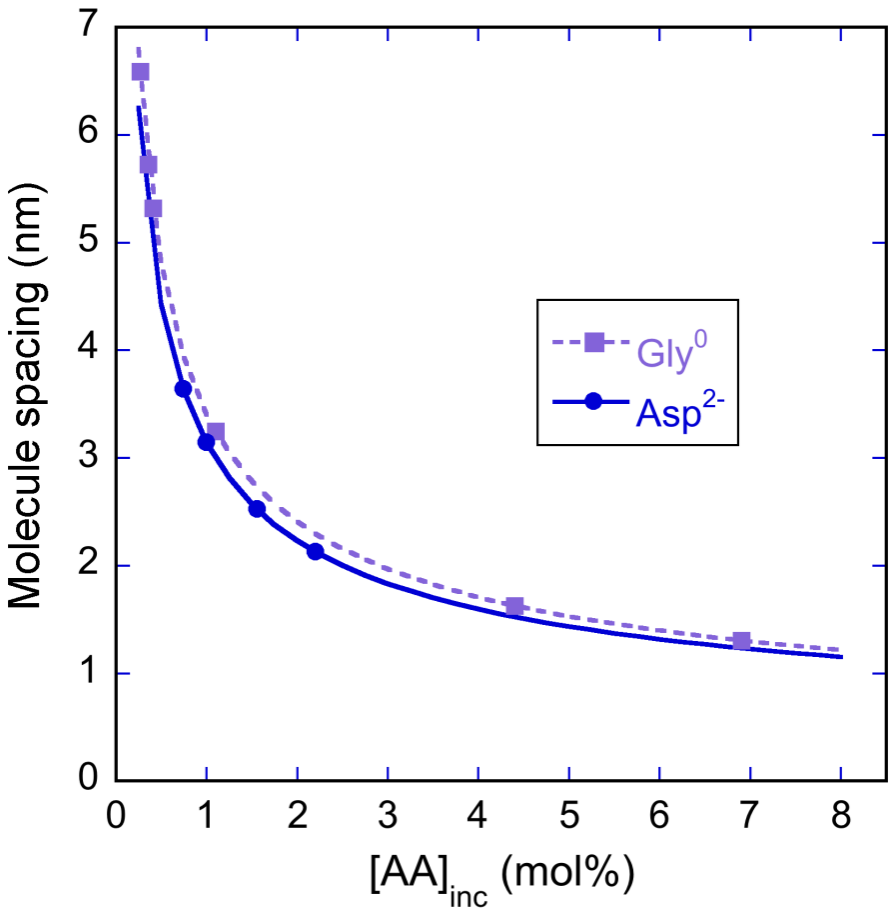

Supplementary Figure 9.

A plot showing intermolecular spacing, *vs.* $[AA]_{inc}$ calculated using Supplementary Equation 5. Symbols indicate the compositions of samples that were mechanically tested in this work.

Supplementary Table 1

XRD structure parameters and their goodness of fitness (GOF) of Asp/calcite and Gly/calcite shown in Fig. 3 as obtained from Rietveld analysis.

AA	conc [mM]	mol%	a(Å)	c(Å)	χ^2	$\Delta a/a$	$\Delta c/c$
Pure	0	0	4.9903	17.063	3.17	0	0
Asp	0.1	0.036	4.9907	17.068	6.355	8.02E-05	2.93E-04
Asp	1	0.5	4.9915	17.076	3.454	2.40E-04	7.62E-04
Asp	5	1.006	4.9921	17.096	18	3.61E-04	1.93E-03
Asp	10	1.673	4.9923	17.105	10.3	4.01E-04	2.46E-03
Asp	50	3.992	4.9927	17.114	11.30	4.81E-04	2.99E-03
Asp	100	2.728	4.9916	17.110	5.71	2.61E-04	2.75E-03
Gly	5	0.28	4.9907	17.069	11.38	8.02E-05	3.52E-04
Gly	10	0.387	4.9908	17.073	26.89	1.00E-04	5.86E-04
Gly	50	1.138	4.9918	17.102	29.85	3.01E-04	2.29E-03
Gly	100	1.707	4.9931	17.120	22.79	5.61E-04	3.34E-03
Gly	200	4.4	4.9931	17.136	15.27	5.53E-04	4.31E-03
Gly	400	6.9	4.9936	17.152	14.36	6.59E-04	5.24E-03

Supplementary Table 2

Goodness of Fitness values obtained from line profile analysis of Asp/calcite and Gly/calcite samples shown in Fig. 3. (a) Asp/calcite samples (b) Gly/calcite samples.

a

Reflection	Asp 1 mM	Asp 10 mM	Asp 5 mM	Asp 50 mM	Asp 100 mM
(012)	1.01	1.87	1.64	0.98	3.00
(104)	4.00	4.56	5.23	3.98	3.82
(006)	0.84	1.05	1.26	0.78	0.78
(110)	1.23	1.48	3.13	0.94	1.13
(113)	1.53	2.40	2.68	1.40	1.43
(202)	1.60	1.47	3.14	1.30	1.21

b

Reflection	Gly 5 mM	Gly 10 mM	Gly 50 mM	Gly 100 mM	Gly 200 mM	Gly 400 mM
(012)	1.19	2.26	1.26	1.05	2.87	2.35
(104)	7.33	7.43	3.88	4.72	11.78	12.18
(006)	0.82	2.11	0.95	0.97	1.56	1.42
(110)	1.42	2.45	2.33	1.96	3.73	2.50
(113)	1.74	1.32	2.48	3.61	5.10	3.32
(202)	0.88	1.39	1.34	5.30	3.57	7.73

Supplementary References

1 Ihli, J., Bots, P., Kulak, A., Benning, L. G. & Meldrum, F. C. Elucidating mechanisms of diffusion-based calcium carbonate synthesis leads to controlled mesocrystal formation. *Adv. Funct. Mater.* **23**, 1965-1973 (2013).

2 Penkman, K. E. H., Kaufman, D. S., Maddy, D. & Collins, M. J. Closed-system behaviour of the intra-crystalline fraction of amino acids in mollusc shells. *Quat. Geochronol* **3**, 2-25 (2008).

3 Demarchi, B. *et al.* Intra-crystalline protein diagenesis (IcPD) in Patella vulgata. part I: isolation and testing of the closed system. *Quat Geochronol* **16**, 144-157 (2013).

4 Tomiak, P. J. *et al.* Testing the limitations of artificial protein degradation kinetics using known-age massive Porites coral skeletons. *Quat Geochronol* **16**, 87-109 (2013).

5 Kaufman, D. S. & Manley, W. F. A new procedure for determining DL amino acid ratios in fossils using reverse phase liquid chromatography. *Quat. Sci. Rev.* **17**, 987-1000 (1998).

6 Demarchi, B. *et al.* New Experimental Evidence for In-Chain Amino Acid Racemization of Serine in a Model Peptide. *Anal. Chem.* **85**, 5835-5842 (2013).

7 Szeverenyi, N. M., Sullivan, M. J. & Maciel, G. E. Observation of spin Exchange by two-dimensional fourier-transform C-13 cross polarization-magic-angle spinning. *J. Magn. Reson.* **47**, 462-475 (1982).

8 Thompson, S. P. *et al.* Beamline I11 at Diamond: a new instrument for high resolution powder diffraction. *Rev. Sci. Instrum.* **80**, 075107 (2009).

9 Oliver, W. C. & Pharr, G. M. Measurement of hardness and elastic modulus by instrumented indentation: advances in understanding and refinements to methodology. *J. Mater. Res.* **19**, 3-20 (2004).

10 Kunitake, M. E., Mangano, L. M., Peloquin, J. M., Baker, S. P. & Estroff, L. A. Evaluation of strengthening mechanisms in calcite single crystals from mollusk shells. *Acta Biomater.* **9**, 5353-5359 (2013).

11 Martinez, L., Andrade, R., Birgin, E. G. & Martinez, J. M. PACKMOL: A package for building initial configurations for molecular dynamics simulations. *J. Comput. Chem.* **30**, 2157-2164 (2009).

12 Wang, J. M., Wang, W., Kollman, P. A. & Case, D. A. Automatic atom type and bond type perception in molecular mechanical calculations. *J. Mol. Graphics Modell.* **25**, 247-260 (2006).

13 Jakalian, A., Jack, D. B. & Bayly, C. I. Fast, efficient generation of high-quality atomic charges. AM1-BCC model: II. parameterization and validation. *J. Comput. Chem.* **23**, 1623-1641 (2002).

14 Todorov, I. T., Smith, W., Trachenko, K. & Dove, M. T. DL_POLY_3: new dimensions in molecular dynamics simulations via massive parallelism. *J. Mater. Chem.* **16**, 1911-1918 (2006).

15 Raiteri, P., Gale, J. D., Quigley, D. & Rodger, P. M. Derivation of an accurate force-field for simulating the growth of calcium carbonate from aqueous solution: a new model for the calcite-water interface. *J. Phys. Chem. C* **114**, 5997-6010 (2010).

16 Wang, J. M., Wolf, R. M., Caldwell, J. W., Kollman, P. A. & Case, D. A. Development and testing of a general amber force field. *J. Comput. Chem.* **25**, 1157-1174 (2004).

17 Freeman, C. L. *et al.* New forcefields for modeling biomineralization processes. *J. Phys. Chem. C* **111**, 11943-11951 (2007).

18 Hoover, W. G. Canonical dynamics - equilibrium phase-space distributions. *Phys. Rev. A* **31**, 1695-1697 (1985).
19 Melchionna, S., Ciccotti, G. & Holian, B. L. Hoover npt dynamics for systems varying in shape and size. *Mol. Phys.* **78**, 533-544 (1993).
20 DeBresser, J. H. P. & Spiers, C. J. Strength characteristics of the r, f, and c slip systems in calcite. *TCTOAM* **272**, 1-23 (1997).
21 Akbulatov, S., Tian, Y. C. & Boulatov, R. Force-reactivity property of a single monomer is sufficient to predict the micromechanical behavior of its polymer. *J. Am. Chem. Soc.* **134**, 7620-7623 (2012).
22 Diesendruck, C. E. *et al.* Mechanically triggered heterolytic unzipping of a low-ceiling-temperature polymer. *Nat. Chem.* **6**, 624-629 (2014).
23 Grandbois, M., Beyer, M., Rief, M., Clausen-Schaumann, H. & Gaub, H. E. How strong is a covalent bond? *Science* **283**, 1727-1730 (1999).
24 Friedel, J. *Les Dislocations*. 72 (Gauthier-Villars, Paris, 1956).
25 Cheng, Y. T. & Cheng, C. M. Scaling approach to conical indentation in elastic-plastic solids with work hardening. *J. Appl. Phys.* **84**, 1284-1291 (1998).
26 Kunitake, M. E., Baker, S. P. & Estroff, L. A. The effect of magnesium substitution on the hardness of synthetic and biogenic calcite. *MRS Commun.* **2**, 113-116 (2012).
27 Moureaux, C. *et al.* Structure, composition and mechanical relations to function in sea urchin spine. *J. Struct. Biol.* **170**, 41-49 (2010).
28 Perez-Huerta, A., Cusack, M., Zhu, W. Z., England, J. & Hughes, J. Material properties of brachiopod shell ultrastructure by nanoindentation. *J. R. Soc., Interface* **4**, 33-39 (2007).
29 Griesshaber, E. *et al.* Crystallographic texture and microstructure of terebratulide brachiopod shell calcite: an optimized materials design with hierarchical architecture. *Am. Mineral.* **92**, 722-734 (2007).
30 Wang, R. Z., Addadi, L. & Weiner, S. Design strategies of sea urchin teeth: structure, composition and micromechanical relations to function. *Philos. Trans. R. Soc., B* **352**, 469-480 (1997).
31 Kim, Y. Y. *et al.* Bio-inspired synthesis and mechanical properties of calcite-polymer particle composites. *Adv. Mater.* **22**, 2082-2086 (2010).
32 Perlovich, G. L., Hansen, L. K. & Bauer-Brandl, A. The polymorphism of glycine - Thermochemical and structural aspects. *J. Therm. Anal. Calorim.* **66**, 699-715 (2001).
33 Anthony, J. W., Bideaux, R. A., Bladh, K. W. & Nichols, M. C. in *Handbook of Mineralogy* Ch. V (Borates, Carbonates, Sulfates), (Mineralogical Society of America, ed. 2003).
34 Bendeif, E. E. & Jelsch, C. The experimental library multipolar atom model refinement of L-aspartic acid. *Acta Crystallogr., Sect. C: Cryst. Struct. Commun.* **63**, O361-O364 (2007).
35 Shannon, R. Revised effective ionic radii and systematic studies of interatomic distances in halides and chalcogenides. *Acta Crystallogr., Sect. A: Found. Adv.* **32**, 751-767 (1976).
36 Eshelby, J. D. The determination of the elastic field of an ellipsoidal inclusion, and related problems. *Proc. R. Soc. London, Ser. A* **241**, 376-396 (1957).
37 Bass, J. D. in *Mineral Physics & Crystallography: A Handbook of Physical Constants* 45-63 (American Geophysical Union, 2013).
38 Clayton, J. D. & Knap, J. Phase field modeling of twinning in indentation of transparent crystals. *Modell. Simul. Mater. Sci. Eng.* **19**, 085005 (2011).
39 Li, L. & Ortiz, C. Pervasive nanoscale deformation twinning as a catalyst for efficient energy dissipation in a bioceramic armour. *Nat. Mater.* **13**, 501-507 (2014).

40 Mullner, P. Between microscopic and mesoscopic descriptions of twin-twin interaction. *Z Metallkd* **97**, 205-216 (2006).
41 Ghazisaeidi, M., Hector, L. G. & Curtin, W. A. Solute strengthening of twinning dislocations in Mg alloys. *Acta Mater.* **80**, 278-287 (2014).